Correlation revival eigenmodes for differential sensitivity in speckle metrology

Hal Gee, Morgan Facchin, and Graham D. Bruce*
SUPA, School of Physics and Astronomy, University of St. Andrews, St. Andrews KY16 9SS, United Kingdom

(Received 10 April 2026; accepted 25 September 2026; published 16 November 2026)

Speckle metrology exploits the high sensitivity of scattered fields to parameters of interest, yet this also leaves measurements vulnerable to unintended perturbations. Here we employ transmission matrix formalism to engineer light fields that produce speckle correlation "revivals," selectively reducing response to chosen parameters. In a multimode fiber scattering system, we first achieve a 40× suppression of bending-induced correlation changes over a limited curvature range, without significantly reducing wavelength sensitivity. We then demonstrate that this approach generalizes easily from one nuisance parameter to two by introducing a polarization-translation perturbation in addition to bending. This methodology opens a route to tailored, parameter-specific sensitivities of speckle-based measurements.

DOI: 10.1103/jl5y-q2q2

I. INTRODUCTION

Coherent light propagates through disordered media to produce highly sensitive, granular patterns known as speckle [1,2]. Speckle is typically an unintentional and unwanted corruptor in imaging systems, and much effort is put into methods for its removal. Its sensitivity, however, makes it difficult to suppress. Even microscopic fluctuations in the properties of the incident light or of the scatterer can cause visibly macroscopic shifts in the resulting speckle. However, this effect can be repurposed to yield highly sensitive measurements in parameters of interest. Simple systems may capture the speckle from a scatterer, extract its variation, and establish a quantitative link between shifts in the speckle and shifts in the perturbing parameter(s) [3]. High sensitivity speckle metrology has been demonstrated for measurement of wavelength [4–8], refractive index [9], strain, deformation and displacement [10–14], and fluid velocity [15].

Across these domains, selectivity is as important as sensitivity. For example, when measuring wavelength, sensitivity to temperature, vibrations, or polarization can be detrimental. There are broadly two ways to cope with this. The system can be isolated from parameters of disinterest, to shield its sensitivity [12,16]. Alternatively, the issue can be shifted into analysis, where only the desired variation is captured [6]. Both of these approaches address symptoms rather than the root cause. To address the problem itself, the speckle produced by a scatterer would need to be made inherently insensitive to certain parameters. To do this, a scattering model is first needed.

The transmission matrix (TM) is one such model. Since the input and output fields of a scatterer are linearly related, the fields can be expressed as vectors in some chosen basis, and the scatterer as a matrix transformation [17,18]. This conceptually simple framework turns complex scattering scenarios into problems of linear algebra whose solutions are often exact, or at worst, can be solved with known techniques. This allows imaging through scattering media [19,20], as well as the calculation of propagation modes with various eigenproperties [21–23]. Of particular interest to metrology are modes insensitive to certain disturbances, such as to fiber bending [24] or wavelength [25]. Particular approaches have been studied, such as Wigner-Smith eigenmodes [25,26], but they are rarely evaluated in concrete metrological contexts with multiple variable parameters.

In the following, we introduce a desensitization approach which leverages nonlocal eigenmodes of the transmission matrix for speckle metrology. The nonlocality manifests as a "revival" in the speckle correlation occuring after an arbitrary perturbation distance. We identify an appropriate form of transmission-matrix-derived operator to realize these revivals, and perform controlled-noise simulations to explore the robustness of the approach. We experimentally demonstrate bending correlation revivals in a commonly used multimode fiber type over a range of curvatures, and show how these modes realize differential sensitivity by reducing the response to curvature changes without significantly reducing the sensitivity to wavelength. Altogether, we highlight a strategy which can be applied to any scattering medium, not only to fibers, without any prior knowledge of the special modes of the medium.

II. CONSTRUCTION OF CORRELATION REVIVALS

Let us work in a one-parameter space where the TM is given as $T(\alpha)$. α may be any physical quantity, and the following will not assume a particular one. The TM takes some static input field to a corresponding output field whose α

*Contact author: gdb2@st-andrews.ac.uk

Published by the American Physical Society under the terms of the Creative Commons Attribution 4.0 International license. Further distribution of this work must maintain attribution to the author(s) and the published article's title, journal citation, and DOI.

dependence arises solely from that of $T(\alpha)$:

$$\vec{a} \in \mathbb{C}^N \underset{T(\alpha)}{\to} \vec{b}(\alpha) \in \mathbb{C}^M.$$

We begin at some origin α_0. The similary metric S used to analyze an arbitrary $\vec{b}(\alpha)$ is the Pearson correlation of intensities between $\vec{b}(\alpha)$ and the initial $\vec{b}(\alpha_0)$. With $|\cdot|^2_\odot$ as the element-wise norm squared

$$S(\alpha) = \mathrm{Corr}[|\vec{b}(\alpha)|^2_\odot, |\vec{b}(\alpha_0)|^2_\odot]. \tag{1}$$

Typically, the goal is to maximize or minimize the sensitivity of $S(\alpha)$ to α in some region around α_0. In contrast to this localized (de)sensitization, we may instead aim to maximize or minimize the effect on $S(\alpha)$ when moving to a specific, remote point α_1. In all that follows, the path of *minimization* is taken [maximization of the effect on $S(\alpha)$ may instead be useful for enhanced sensitivity]. Specifically, we desire $S(\alpha_1) = S(\alpha_0) = 1$. It will be convenient to denote these correlations S_1 and S_0, respectively, and likewise for $\vec{b}_1$ and $\vec{b}_0$.

S_0 is 1 by definition, as it is the correlation of $\vec{b}_0$ with itself. As a simple first approach, we may try to force $S_1 = 1$ by using precisely the same reasoning. If we engineer an $\vec{a}$ that causes $\vec{b}_1 = \vec{b}_0$, then S_1 is the same self-correlation. This is arguably overconstrained because only the *intensities* need to correlate, not necessarily the *fields*, but this is mathematically more approachable.

We proceed very simply as follows:

$$\begin{aligned} T_0\vec{a} &= T_1\vec{a} \\ &\Rightarrow (T_1 - T_0)\vec{a} = \vec{0} \\ &\Rightarrow \vec{a} \in \ker(T_1 - T_0). \end{aligned}$$

If the system is overdetermined, requiring $M < N$, then $\ker(T_1 - T_0)$ will have a nontrivial size. Constraining $\vec{a}$ to the unit sphere of this space, we may then choose the $\vec{a}$ whose outputs $\vec{b}_0$ and $\vec{b}_1$ have the greatest power. This is done primarily to keep the measurement signal-to-noise ratio (SNR) high.

Since $\vec{b}_0 = \vec{b}_1$, the average output power is given as

$$\bar{P} = \tfrac{1}{2}|b_0|^2 + \tfrac{1}{2}|b_1|^2 = |b_0|^2 = |T_0\vec{a}|^2.$$

If B is a semi-unitary matrix whose columns span the kernel, then $\vec{a} = B\vec{v}$ for some unit $\vec{v}$, and $\bar{P} = |T_0 B\vec{v}|^2$.

The overall process is therefore to compute the singular value decomposition (SVD) of $T_1 - T_0$ in order to form B, and then to compute the SVD of T_0B, whose dominant right-singular vector $\vec{v}_{\max}$ must maximize $\bar{P}$:

$$\vec{v}_{\max} = \underset{\vec{v},|\vec{v}|=1}{\mathrm{argmax}} |T_0 B\vec{v}|^2, \quad \vec{a}_{\max} = B\vec{v}_{\max}. \tag{2}$$

In this way we find the desired revival input field $\vec{a}_{\max}$. It is easy to extend this to multiple revivals at TMs T_n by forming the stacked matrix

$$\Delta_{\mathrm{stack}} = \begin{bmatrix} T_1 - T_0 \\ \vdots \\ T_n - T_0 \end{bmatrix},$$

and instead computing B to span $\ker(\Delta_{\mathrm{stack}})$ via SVD.

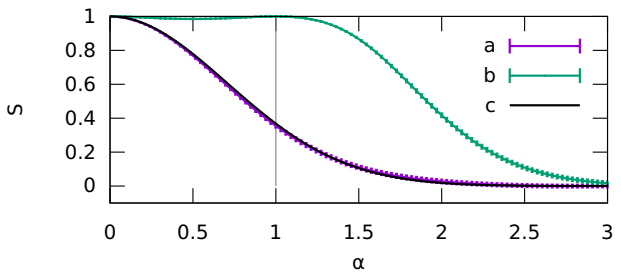


FIG. 1. Simulated correlation curves for phase-only $T(\alpha)$, (a) without and (b) with an engineered revival at $\alpha = 1$. Without a revival, the form of $S(\alpha)$ is known, and this is also shown (c). One hundred simulations are averaged for curves (a) and (b).

We have left the behavior of $S(\alpha)$ unspecified between α_0 and α_1, so it is not clear how $\vec{a}_{\max}$ might effect its overall form. The effect on $\bar{P}$ in comparison to the output power of a random $\vec{a} \in \mathbb{C}^N$ is also unclear. The latter problem can be analyzed given certain assumptions on $T(\alpha)$. In fact, it can be shown that for i.i.d. complex Gaussian $T(\alpha_0)$ and $T(\alpha_1)$ if nothing is done to boost $\bar{P}$, we expect it to be half of that for random input (Appendix A).

III. SIMULATION

We can create a simple simulation by assuming that

$$\begin{aligned} T_{mn}(\alpha) &= \exp(i\varphi_{mn} + i\alpha\theta_{mn}), \\ \varphi_{mn} &\sim \mathcal{U}[0, 2\pi), \quad \theta_{mn} \sim \mathcal{N}(0, 1). \end{aligned} \tag{3}$$

This represents a scatterer with lossless independent paths, each having an inherent phase shift and one linear in α (imitating path length dependence on wavelength).

T is chosen to be 400×512 to give significantly more input degrees of freedom (DOFs) than output DOFs. This ensures that we draw $\vec{a}$ from a large kernel, a precaution we would take in experiment to increase robustness against measurement errors that may tilt the solution space. Revivals will be induced between $\alpha = 0$ and a variable critical value α_{crit}. α will then be swept from 0 beyond α_{crit} to yield a smooth $S(\alpha)$ curve computed with Eq. (1). To reduce noise, we average over 100 simulations with different φ_{mn} and θ_{mn}.

Figure 1 shows the revival curve $S(\alpha)$ for $\alpha_{\mathrm{crit}} = 1$, compared with the curve for a random input field. The latter can be derived to have the form $\exp(-\alpha^2)$ (Appendix B). The revival shows remarkable flatness between its peaks, representing significant insensitivity to α. This suggests that the response of a system may indeed be made to resist a certain parameter of (dis)interest. However, we must also examine the effectiveness of this insensitivity as we attempt to widen the revival further.

A simple metric for this examination is the correlation at the "dip" between the two peaks: $S(\alpha_{\mathrm{crit}}/2)$. The dip is negligible for small α_{crit}, and $S(\alpha_{\mathrm{crit}}/2)$ must tend to 0 once the peaks are distant enough to have little crossover.

Figure 2(a) arrays many revival curves like that of Fig. 1, but at different α_{crit} values, to show the widening central dip. Figure 2(b) shows the value of $S(\alpha_{\mathrm{crit}}/2)$ by cross sectioning the graph of Fig. 2(a) along the marked line. An analytic form for this curve was not known, but it is described well

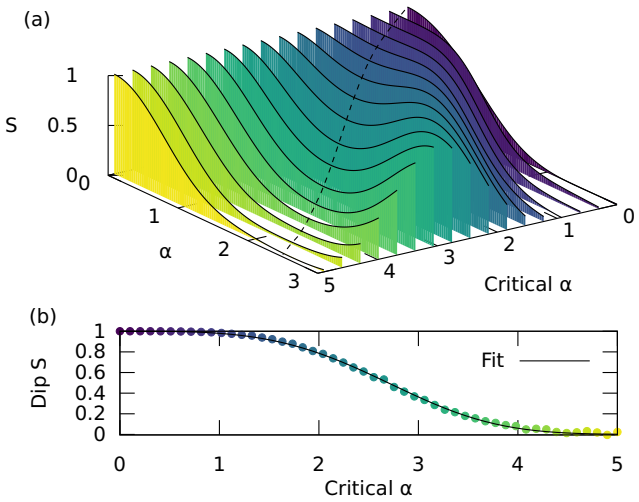


FIG. 2. (a) Revival curves for different critical α values, with the dip between peaks marked by a dashed line. Each curve is the average of 100 simulations. (b) Correlation value at these dips against critical α, showing values obtained from the data in (a) as well as a super-Gaussian fit.

by a super-Gaussian fit of exponent 1.75 ± 0.024, standard deviation 2.12 ± 0.006. Inspecting these values reveals that the data strongly fits a stretched exponential

$$S_{\text{dip}} = \exp(-(\alpha_{\text{crit}}/3)^{\frac{7}{2}}).$$

The high exponent gives a flattened top to this curve, where 95% of the correlation is maintained up to $\alpha_{\text{crit}} = 1.3$, at which point the half-width at half maximum (HWHM) of the revival curve is more than doubled (215%).

While in principle this appears powerful, its robustness against noise will determine experimental viability. In particular, the measured values of T will differ from truth by some error on every element, and therefore the $\vec{a}_{\text{max}}$ we compute will not cause a full revival in $S(\alpha)$.

As a simplistic error model, we apply an additive perturbation to T to give $T' = T + E$, with i.i.d. circular Gaussian entries in E. E is different for each measurement of T. To simulate this, the revival input $\vec{a}$ is generated for the perturbed TMs, $T(0) + E_0$ and $T(\alpha_{\text{crit}}) + E_1$, and the intensity correlation is then computed between the unperturbed $\vec{b}_0 = T_0\vec{a}$ and $\vec{b}_0(\alpha) = T(\alpha)\vec{a}$. Figure 3(a) shows the effect of this error scheme. The revival peak is dampened as noise is added, and when its height is plotted in Fig. 3(b), we find it is the fourth power of the correlation between the perturbed and unperturbed TMs:

$$S_{\text{peak}} = (S_{\text{TM}})^4.$$

This result can be found analytically (Appendix C). Intuitively, S_{peak} is high order in S_{TM} for two reasons. First, the peak revival field correlation is between two fields both affected by TM inaccuracy, whereas S_{TM} is between an inaccurate TM and its true value, giving a second-power relation of the former over the latter. Second, revival correlation is measured in intensity, and by the Siegert relation, this is an additional squaring of the field correlation, thus giving a fourth power in total.

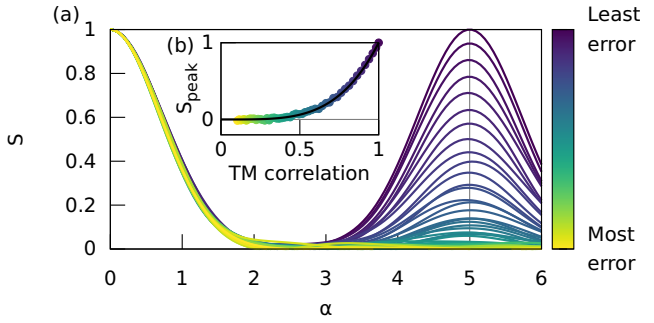


FIG. 3. (a) Effect on $S(\alpha)$ of error added to TMs, for $\alpha_{\text{crit}} = 5$. (b) $S(\alpha_{\text{crit}})$ vs correlation between $T(0)$ and $T(0) + E_0$, showing datapoints from simulation as well as a quartic fit.

The unfortunate conclusion of this last simulation is that even quite accurate TM measurements lead to imperfect revivals. With 90% correlation between subsequent TM measurements, we expect only 66% revival height.

IV. COMPARISON WITH WIGNER-SMITH OPERATOR

Our procedure bears a close connection to the generalized Wigner-Smith operator [26], which has been widely used to construct parameter-insensitive transmission channels. It is therefore important to clarify whether the two approaches are equivalent, and if not, what practical advantages arise from the present construction.

Modes obtained from the generalized Wigner-Smith operator arise as eigenvectors of

$$W = T_0^{-1}(T_1 - T_0).$$

The full eigenspectrum is meaningful; for eigenvector $\vec{a}$ with eigenvalue τ, we observe that

$$(\tau + 1)T_0\vec{a} = T_1\vec{a},$$

and thus that the two output fields only differ in scale. This gives a larger solution space than does our procedure if one is only interested in obtaining revivals in S of 1 under ideal conditions. However, there are three important differences which each lead the Wigner-Smith approach to perform worse for our goals.

(1) A suitable inverse T_0^{-1} is required. This inversion is notoriously susceptible to noise when T_0 has small singular values, and the usual approach is a truncated pseudoinverse [25]. Truncation here means that singular values σ_i of T_0 are discarded (along with their vectors) if $|\sigma_i| < t|\sigma_{\text{max}}|$, where $0 \leqslant t < 1$, typically 0.1. Not only does this add more computation (SVD + inverse), it gives a mode error rising with t because every deleted singular vector mixes a spurious null dimension into W.

(2) As τ increases, the dip between the revival peaks deepens. For our metrological purposes, we are attempting to create a flat reponse, and any effect analogous to passband ripple is undesirable.

(3) Existing Wigner-Smith schemes do not perform the power maximization of Eq. (2). In addition to improving the measurement SNR, this appears to slightly decrease

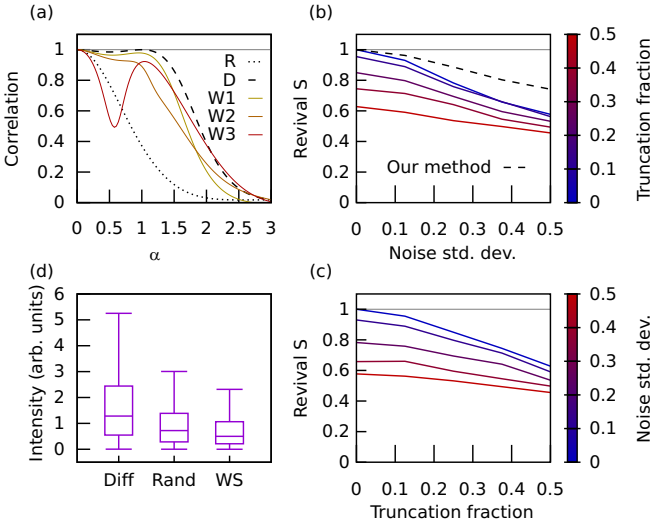


FIG. 4. (a) Correlation responses for different input modes: random circular gaussian (R), our method (D), and Wigner-Smith with $\tau = 0$ (W1), $\tau = \tau_{\max}/2$ (W2), and $\tau = \tau_{\max}$ (W3). W modes have truncation $t = 0.1$. (b) Revival peak height as TM noise increases, for several truncation t values. (c) Likewise, but against t for different TM noise levels. (d) Output intensity distributions, showing quartiles and clipped 1.5 IQR whiskers, where $t = 0.1$ for WS. All data points of (a), (b), or (c) are means over 100 simulations with 100×128 TMs. In (d), a 1000×1280 TM was used. All TMs were generated according to Eq. (3).

vulnerability to TM noise, and slightly increase flatness in the passband.

These effects can be easily explored in simulation.

When $\tau = t = 0$, solutions are drawn from $\ker(W)$, and the solution space is the same as ours but for power maximization. In this degenerate case, computing T_0^{-1} has no benefit, and so our scheme is preferable. In practice however, one raises t per point 1 to stabilize W, and even in the absence of measurement noise, we incur error in the modes from $\ker(W)$ as shown in Figs. 4(b) and 4(c).

For $\tau > 0$, Fig. 4(a) clearly shows that the correlation passband becomes uneven, and moreover, that the peak height is more susceptible to the effect of the same $t > 0$.

Finally, Fig. 4(d) shows that the output intensity distribution arising from a Wigner-Smith input mode is substantially weaker than that resulting from our method, as well as from a random input. This has only a small effect on measurement noise, but is worth consideration.

Taken together, it can be inferred from these results that to obtain revivals of equal quality using our method and the Wigner-Smith operator, increased demands on measurement accuracy affect the latter. This is to compensate for the effects of constructing a suitable pseudoinverse and not incorporating power maximization.

V. EXPERIMENTAL VERIFICATION

To experimentally demonstrate speckle revivals, we use a Digital Micromirror Device (DMD) to imprint desired wavefronts onto a 785-nm laser beam, while the variable TM is that of a step-index, 200 μm core multimode fiber.

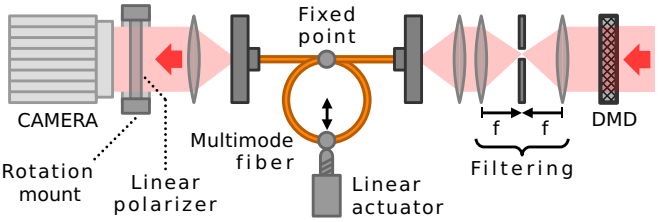


FIG. 5. Simplified experimental setup. A collimated beam is incident on the DMD, whose first order diffraction is Fourier-filtered to create the target wavefront. This is sent into a deformable multimode fiber, recollimated at the far end, linearly polarized, and imaged directly onto a camera.

Figure 5 shows an idealized representation of the system. This setup allows direct intensity measurement of the output of the fiber TM, restricted to one polarization such that the field is fully self-interfering. All major components are shown in Appendix D.

The DMD is aligned such that off-state mirrors face the incoming beam, as recommended by the diffraction grating analysis in [27]. In our case, this is 12°.

The micromirror array is divided into 512 regions in a rectangular grid. Each region corresponds to one complex DOF after filtering, accomplished by the generation of binary holograms [28] using the recent "superpixel" method [29], with an original computational approach centered on *k-d* tree spatial lookup. With each region composed of repeated 4×4 cells, the unit disk in $\mathbb{C}$ is split into 6561 achievable points for each DOF. Hologram projection is synchronized to the camera, so that every falling edge of its exposure signal causes a DMD update.

We measure TMs with a Hadamard input basis. This orthogonal basis, whose vector elements are ± 1, is often used as a basis for TM measurement due to its ability to excite scatterer modes more favorably than, e.g., Fourier basis fields [30]. The probe inputs are added to a uniform value-1 field before being sent through the fiber. This results in an output field that is the sum of two speckle fields: one due to each probe, and one due to the uniform field. The latter can be used as a nonuniform reference to make interferometric measurements of the former [31]. This "copropagating" reference scheme avoids the stability issues associated with reference arm topologies.

The 512 input DOFs are covered by 512 probe patterns. Each is shown four times with a different global phase, shifted in increasing multiples of $\pi/2$. This allows interferometric recovery of the complex value of the output field [32]. To obtain the desired 400 output values, the reference speckle is measured first, and 400 points are selected by descending brightness, requiring that no point is within one speckle grain of another. These locations form a subsampling mask for further measurements. In this way, each probe produces one column of the Hadamard-basis TM. This is converted back to direct basis by post-multiplication with the inverse of the Hadamard pattern matrix.

We demonstrate speckle correlation revivals with respect to fiber bending. A loop of fiber (circumference 31 cm) is fixed at its self-crossing point, and the opposing point on the loop

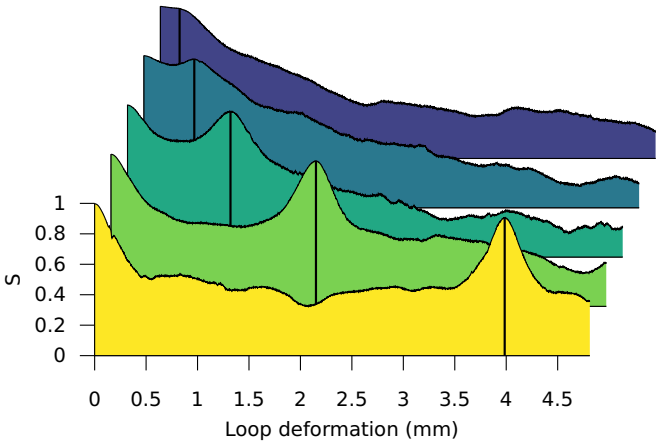


FIG. 6. Revivals over several distances. Back to front, peaks are set at 0.2, 0.5, 1, 2, and 4 mm deformation. Axes are identical.

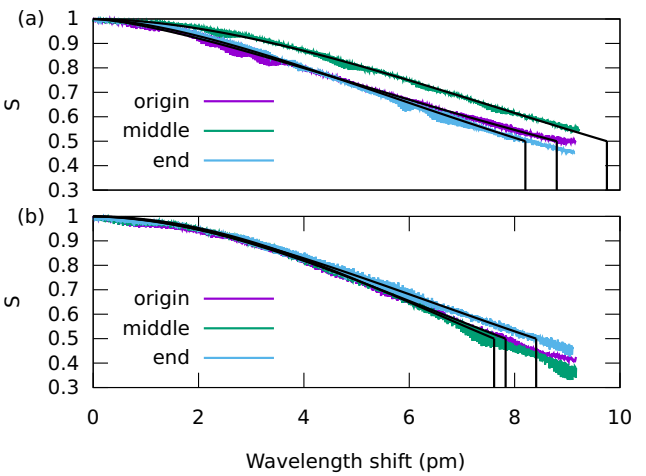


FIG. 7. (a) Correlation responses to wavelength for a revival input field. (b) Likewise for a random circular Gaussian input field. "Origin," "middle," and "end" correspond to 0, 1, and 2-mm deformation. The revival peak was positioned at 2 mm.

is mounted to a linear actuator. Actuator motion deforms only the looped part of the fiber (Fig. 5).

Initially, the loop sits roughly circular. The first reference speckle is measured, the actuator moves to the target deformation, and the second reference speckle is measured. As above, a subsampling mask is chosen, but here we must choose points by descending minimum brightness between the two references, so that all points show adequate interference at both positions. T_0 and T_1 are then acquired at the initial and target deformations. The revival input field is computed with Eq. (2). The actuator returns to the origin, and projection of the revival field begins. The actuator slowly bends the fiber to the target displacement while video is recorded from the camera.

To generate correlation curves, each frame in a video is subsampled with the same mask as for TM measurement, before its correlation to the first frame is computed.

Revivals were generated at various deformations, as shown in Fig. 6. The typical peak S ranged from 0.9 to 0.97, indicating TM error of 1% to 3% under our earlier model.

While revivals in the speckle field are observed when the design parameter (fiber bending) varies, we now ask whether this revival may have side effects on the speckle response to other parameters, such as wavelength. With a revival field in place, correlation curves were measured against wavelength at different deformations [Fig. 7(a)] by scanning over 10 pm bidirectionally at least four times. The same was done for a random, circular Gaussian input field [Fig. 7(b)]. The mean HWHMs are 8.92 and 7.95 pm, respectively, 12% wider for the revival field. This represents only a small loss of spectral sensitivity.

The results in Fig. 6 indicate that it is possible to generate a correlation curve with respect to fiber deformation that exhibits a region of very low derivative, suggesting reduced sensitivity to bending over a range of curvatures (for example, the revival centred at 2 mm shows a notably flat response between approximately 0.7 and 1.3 mm). The simulations in Fig. 2 imply that considerably wider regions of reduced sensitivity may be achievable under ideal conditions. Meanwhile, Fig. 7 shows that, for the same input field, the response to wavelength (quantified through the HWHM of the wavelength-correlation curve) is only modestly broadened relative to that of a random input field. We further test this idea by inducing a "double-revival" to force flatness over a particular region. We must increase TM size such that Δ_{stack} has a nontrivial kernel, and we now choose 400×1024. With very close peaks, high correlation is maintained far beyond the width of the response for a random input field (Fig. 8). We quantify our results with the sensitivity ratio

$$R_{\lambda x} = \left|\left(\frac{d\lambda}{dx}\right)_S\right| = \left|\frac{\partial S}{\partial x}\Big/\frac{\partial S}{\partial \lambda}\right|,$$

where x is fiber deformation and λ is wavelength shift. This gives an equivalent error in wavelength due to deformation, and will be evaluated for maximal $|\partial S/\partial\lambda|$. We want this value to be as small as possible.

For the field generating the frontmost curve of Fig. 8, maximal $|\partial S/\partial\lambda|$ was found to be $(53 \pm 1)\text{nm}^{-1}$. In the flattest region (0 to 0.5 mm) and the following linear part (0.5 to 3 mm), we have $R_{\lambda x} = (0.86 \pm 0.02)$ pm/mm and (5.04 ± 0.10) pm/mm, respectively. In stark contrast, the no-revival curve reaches an $R_{\lambda x}$ of more than 37 pm/mm well before we pass 0.5 mm deformation. If we stay within this

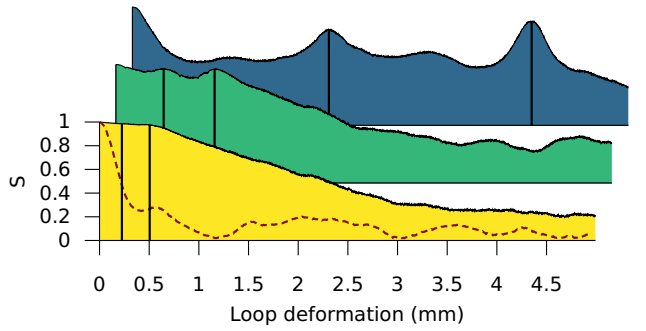


FIG. 8. Deformation double revival as peaks are brought closer. Back to front, peaks are set at multiples of 2, 0.5, and 0.25 mm. Axes are identical. The response for a random, circular Gaussian input field is plotted for comparison (dashed line).

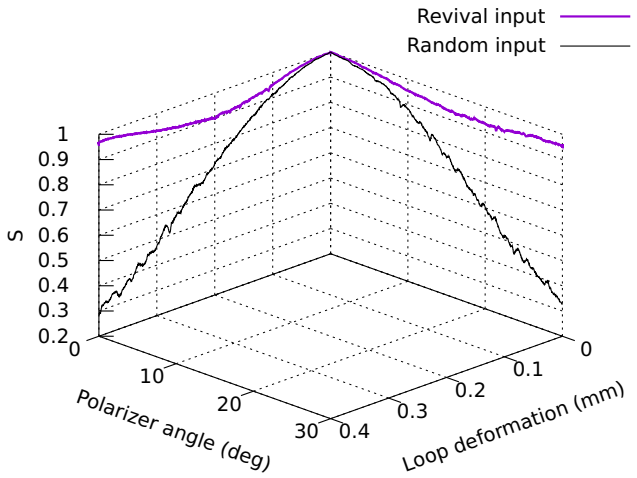


FIG. 9. Two-parameter revival in fiber bending and combined polarization-translation shift. The revivals are designed to occur exactly at the maximal extent shown for each parameter. The correlation responses in both parameters for a random, circular Gaussian input field are also shown for comparison.

region, the revival curve improves our worst $R_{\lambda x}$ by a factor of more than 40. Moving out into the 3-mm region, improvement is by a factor of at least 7.

VI. MULTIPARAMETER EXTENSION

The success of the double revival in one parameter may lead one to try to design a field capable of single revivals in two separate parameters. The design process is precisely the same: forming Δ_{stack} and the matrix B whose columns span its kernel, and solving Eq. (2). The difference is in the functional nature of the TMs, now $T(\alpha, \beta)$ instead of simply $T(\alpha)$. Rather than choosing three α stops $\alpha_0, \alpha_1, \alpha_2$, we choose two α stops and two β stops, defining a rectangle in parameter space bounded by (α_0, β_0) and (α_1, β_1). We measure at least the TMs $T(\alpha_0, \beta_0)$, $T(\alpha_0, \beta_1)$, and $T(\alpha_1, \beta_0)$. The designed field should then show maintained correlation moving from (α_0, β_0) toward either adjacent corner of the domain.

Experimentally, we use the rotation of the linear polarizer (Fig. 5) as an additional parameter, arranged so that, in addition to polarization, a cyclic translation effect occurs. This effect cycles on 360° of the polarizer angle, whereas the polarization cycles on 180°. This gives a faster decorrelation than polarization alone. We also lower the TM size to 200×512 to show that the number of DOFs is not critical, provided the input-output ratio exceeds the revival count.

Figure 9 shows that this type of split double-revival is just as viable as the straightforward version in our previous experiment. The fact that the perturbation is physically split does not enter into the theoretical backing, and in fact, one could treat the path taken through parameter space in Fig. 9 as a contour driven by a single arc-length parameter, along which we place two revivals as before.

Figure 10 shows that the wavelength response under the generated revival field incurs a small sensitivity penalty in line with previous observations. In this case, the HWHM of the best fit curve moves from 7.08 pm to 7.81 pm, an increase of approximately 10%.

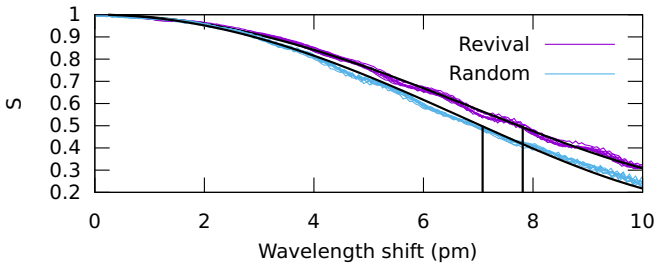


FIG. 10. Comparison of wavelength responses to the revival input field of Fig. 9 and to a random circular Gaussian input. These data are taken at the origin of Fig. 9 in both cases. The two response curves each consist of four bidirectional wavelength sweeps, on top of which is a smooth fit line in black.

VII. CONCLUSION

The above observations show that it is categorically possible to engineer input fields that substantially reduce sensitivity to bending and other disturbances in a way that does not ultimately compromise wavelength sensitivity. Such selective desensitization would be advantageous for the robustness of speckle-based wavemeters, and should, in principle, be extendable to any parameters, as the theory does not rest on any specific choice.

Revival quality, and thus desensitization ability, hinges on TM accuracy. This is impacted by intensity measurement errors as well as scatterer repeatability. Error is minimized by choosing appropriate camera settings to control nonlinearity, and by isolating the system from uncontrolled perturbations during TM measurement.

There is an additional noise effect at the analytical stage: error in the correlation. The standard error of the correlation S for M samples can be estimated [33] as

$$\sigma_S(S, M) = \frac{1 - S^2}{\sqrt{M - 3}}.$$

At a midlevel correlation of 0.5, with 400 output DOFs, we expect $\sigma_S = 0.0376$, or 7.5% error. This is not minor. σ_S accounts well for the smooth noise on experimental correlation curves, and this gives sufficiently large local extrema to affect attempts to desensitize to the revival parameter. To halve σ_S, we must quadruple M, severely expanding measurement and computation time.

We have introduced and experimentally explored a transmission matrix-based method for engineering "revivals" in speckle correlation at selected points in a parameter space. By drawing input fields from the kernels of differences between transmission matrices, we demonstrated that the output speckle can be made substantially less sensitive to bending of a multimode fiber over a finite interval. Simulations indicate that much broader desensitization may be achievable in ideal conditions, although experimental realization is predicated on transmission matrix accuracy, scatterer repeatability, and statistical noise. Measurements show that, for an engineered input field, the slight damping of the spectral correlation bandwidth is more than compensated for by desensitization to bending. Improvements were seen in the sensitivity ratio between these parameters by a factor of over 40 in a narrow

bending scheme (<0.5 mm), and over 7 in a wider scheme (<3 mm). Such control of speckle response is vital for speckle metrology, where robustness to one variable and sensitivity to another are jointly required. More generally, this approach may provide a route toward designing input fields with tailored, parameter-specific responses in scattering systems.

AKNOWLEDGMENTS

H.G. acknowledges support from the Engineering and Physical Sciences Research Council (EPSRC) through the Doctoral Training Partnership Grant No. EP/W524505/1. We thank Kishan Dholakia for useful discussions and comments on the manuscript.

DATA AVAILABILITY

The data that support the findings of this article are openly available [34].

APPENDIX A: EXPECTED REVIVAL OUTPUT POWER FOR INDEPENDENT GAUSSIAN TMS

This scheme suits nonunitary, highly disordered TMs, with revivals created over substantial distances. We model the TMs as complex Gaussian:

$$T_0, T_1 \sim \mathbb{C}\mathcal{N}^{M\times N}\left(0, \sigma_T^2\right).$$

For a revival input $\vec{a}$, the average output power is

$$\bar{P}(\vec{a}) = \tfrac{1}{2}|T_0\vec{a}|^2 + \tfrac{1}{2}|T_1\vec{a}|^2 = |T_0\vec{a}|^2.$$

We can define the sum and difference matrices

$$\Sigma = \frac{T_0 + T_1}{\sqrt{2}} \text{ and } \Delta = \frac{T_0 - T_1}{\sqrt{2}}.$$

These are orthogonal combinations of the two TMs, and they are therefore uncorrelated. For complex Gaussian variables, that is sufficient for their independence. We can use this to rewrite $\bar{P}$, making use of $\vec{a} \in \ker(\Delta)$:

$$\bar{P}(\vec{a}) = \tfrac{1}{2}|(\Sigma + \Delta)\vec{a}|^2 = \tfrac{1}{2}|\Sigma\vec{a}|^2.$$

$\vec{a}$ only depends on Δ, so the expectation of $\bar{P}$ is independent over Σ and $\vec{a}$. With no covariance structure in the TMs, the orientation of $\ker(\Delta)$ is uniform, meaning that $\vec{a}$ covers the unit sphere in $\mathbb{C}^N$ uniformly. Therefore,

$$E[\bar{P}(\vec{a})] = \tfrac{1}{2}E[|\Sigma\vec{a}|^2] = \tfrac{1}{2}M\sigma_T^2.$$

The variance σ_T^2 appears because Σ, by construction, has exactly the same distribution as the TMs. If we instead use a vector $\vec{u} \in \mathbb{C}^N$ chosen uniformly from the unit sphere, then the power becomes

$$E[\bar{P}(\vec{u})] = \tfrac{1}{2}E[|T_0\vec{u}|^2 + |T_1\vec{u}|^2].$$

$\vec{u}$ is independent of both TMs, and therefore the two power expectations are equal:

$$E[\bar{P}(\vec{u})] = \tfrac{1}{2}\left(M\sigma_T^2 + M\sigma_T^2\right) = M\sigma_T^2.$$

Therefore it has been shown that

$$E[\bar{P}(\vec{a})] = \tfrac{1}{2}E[\bar{P}(\vec{u})].$$

APPENDIX B: FORM OF THE SIMULATED CORRELATION CURVE WITHOUT REVIVAL

We have a TM $T(\alpha)$ defined as in Eq. (3), of size $M \times N$. We wish to find analytically $S(\alpha)$.

We may first assume that T has very many columns, and therefore invoke the central limit theorem to say that elements of the output field $\vec{b}(\alpha)$ are circular Gaussian. Under this condition, we may then use the Siegert relation, which for circular Gaussian vectors $\vec{b}_0$ and $\vec{b}_1$ may be stated as

$$\mathrm{Corr}[|\vec{b}_{0,k}|^2, |\vec{b}_{1,k}|^2] = |\mathrm{Corr}[\vec{b}_{0,k}, \vec{b}_{1,k}]|^2. \tag{B1}$$

This is $S(\alpha)$. The task is now to compute the latter correlation. Central to this is the covariance of the same parameters, whose expectation is

$$E\left[\left(\sum_m (T_0)_{km}a_m\right)^*\left(\sum_n (T_1)_{kn}a_n\right)\right] = E\left[\sum_{mn} a_m^* a_n (T_0)_{km}^* (T_1)_{kn}\right],$$

where m, n both run across columns of T. Since $\vec{a}$ is chosen entirely independently of T when not performing a revival, this expectation can be split into

$$\sum_{mn} E[a_m^* a_n]E[(T_0)_{km}^*(T_1)_{kn}^*].$$

Choosing $\vec{a}$ uniformly on the unit sphere results in this expectation vanishing unless $m = n$, leaving only

$$\sum_m \frac{1}{N}E\left[(T_0)_{km}^*(T_1)_{km}^*\right].$$

In our case, where elements of the TM are i.i.d., this is a sum of N identical terms, and must collect simply to

$$E[(T_0)_{11}^*(T_1)_{11}] = E[\exp(i(\alpha_1 - \alpha_0)\theta_{11})],$$

where the element definition from Eq. (3) has been used.

At this point, the subscripts will be dropped, as all θ are i.i.d. We will also let $\alpha = \alpha_1 - \alpha_0$ for convenience. This expectation is, in fact, the characteristic function of the distribution of θ, evaluated at α. For the distribution $\mathcal{N}(0, 1)$, this is known to be $\exp(-\alpha^2/2)$, and so

$$\mathrm{Cov}[\vec{b}_{0,k}, \vec{b}_{1,k}] = \exp\left(-\tfrac{1}{2}\alpha^2\right).$$

From this covariance, we can move directly to the correlation by noting that the correlation must be 1 when $\alpha = 0$, and that the variances of the two parameters to this covariance do not individually depend on α. Those variances would only serve to scale by a constant factor, and the above is already scaled correctly, therefore

$$\mathrm{Corr}[\vec{b}_{0,k}, \vec{b}_{1,k}] = \exp\left(-\tfrac{1}{2}\alpha^2\right).$$

This is inserted into Eq. (B1) to yield

$$S(\alpha) = \exp(-\alpha^2).$$

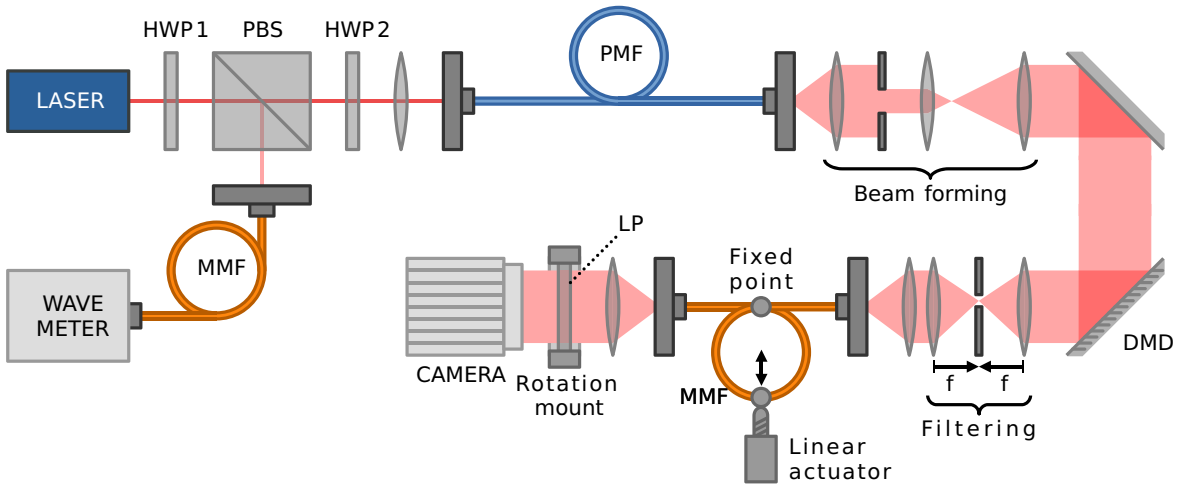


FIG. 11. Schematic of the optical system. The laser beam is first split by a polarizing beamsplitter (PBS) to send ∼2% of its power (controlled by half-wave plate HWP (1) to the wavemeter for wavelength measurement. The rest of the beam is coupled via polarization-maintaining fiber (PMF) into beam-forming optics, consisting of a collimating lens, a circular aperture, and an expansion telescope. This shapes the fiber output into uniform, collimated illumination. The beam then reflects from the DMD into a Fourier filtering stage, which together give holographic phase and amplitude control. The filter aperture consists of an iris opened to ∼1 mm diameter, and $f = 15$ cm. The filtered beam is coupled into the deformable multimode fiber (MMF) whose transmission matrices are to be measured. On exiting the fiber, the light is recollimated, polarized (linear polarizer LP at a computer-controllable angle), and imaged directly onto the sensor of the camera.

APPENDIX C: EFFECT OF TM CORRELATION ON REVIVAL PEAK CORRELATION

We begin by assuming that $T(\alpha_0)$ and $T(\alpha_1)$ are not well correlated. In other words, α_1 is bigger than α_0 by several half-widths of the equivalent revival-less curve. These TMs are denoted T_0 and T_1, respectively.

Additive Gaussian noise is generated as the matrices E_0 and E_1 whose entries are i.i.d., and these create the perturbed TMs $T_0{}' = T_0 + E_0$ and $T_1{}' = T_1 + E_1$. A revival input field $\vec{a}$ is found that gives a joint output field $\vec{b} = T_0\vec{a} = T_1\vec{a}$, with $|\vec{a}| = 1$. We wish to find the correlation

$$S_{\text{output}} = \text{Corr}[|(T_0{}'\vec{a})_k|^2, |(T_1{}'\vec{a})_k|^2]. \tag{C1}$$

We will again use the Siegert relation of Eq. (B1), with the same justification. The covariance we require is

$$\begin{aligned}\text{Cov}[(T_0{}'\vec{a})_k, (T_1{}'\vec{a})_k] &= E[(T_0{}'\vec{a})_k^*(T_1{}'\vec{a})_k] \\ &= E[(\vec{b} + E_0\vec{a})_k^*(\vec{b} + E_1\vec{a})_k] \\ &= E[|b_k|^2 + (E_0\vec{a})_k^* b_k + (E_1\vec{a})_k b_k^* \\ &\quad + (E_0\vec{a})_k^*(E_1\vec{a})_k].\end{aligned}$$

The expectations over E_0 and E_1 are zero, so only the first term contributes. Therefore

$$\text{Cov}[(T_0{}'\vec{a})_k, (T_1{}'\vec{a})_k] = E[|b_k|^2].$$

The elements of the TM are i.i.d. with some variance σ_T^2, and due to the assumption that T_0 and T_1 are highly independent, $\vec{a} \in \ker(T_1 - T_0)$ is sufficiently uncorrelated to T_0 that it acts like any random unit vector, and so

$$E[|b_k|^2] = E[|(T_0\vec{a})_k|^2] = \sigma_T^2.$$

We go about the variances in the same way, starting with

$$\text{Var}[(T_0\vec{a})_k] = \sigma_T^2 + E[|(E_0\vec{a})_k|^2].$$

If the variance of entries of E_0 is σ_E^2 and they are independent from $\vec{a}$, it is similarly the case that

$$E[|(E_0\vec{a})_k|^2] = \sigma_E^2,$$

therefore

$$\text{Var}[(T_0{}'\vec{a})_k] = \sigma_T^2 + \sigma_E^2,$$

and symmetrically so for $T_1{}'$. Finally, placing all of this into Eq. (C1), we find that

$$S_{\text{output}} = \left(\frac{\sigma_T^2}{\sigma_T^2 + \sigma_E^2}\right)^2. \tag{C2}$$

This is a squared Lorentzian in σ_E with half-width σ_T.

The TM correlation is easier, and is expressed as

$$S_{\text{TM}} = \text{Corr}[\text{vec}(T_0)^*, \text{vec}(T_0{}')].$$

TM elements are i.i.d., so we need only take one representative to find the covariance, such as element kl, i.e.,

$$\begin{aligned}\text{Cov}[(T_0)_{kl}^*, (T_0{}')_{kl}] &= E[|(T_0)_{kl}|^2 + (T_0)_{kl}^*(E_0)_{kl}] \\ &= E[|(T_0)_{kl}|^2] \\ &= \sigma_T^2.\end{aligned}$$

Meanwhile, the variances are trivially

$$\text{Var}[(T_0)_{kl}] = \sigma_T^2 \text{ and}$$

$$\text{Var}[(T_0{}')_{kl}] = \sigma_T^2 + \sigma_E^2.$$

The correlation is then

$$S_{\text{TM}} = \frac{\sigma_T}{\sqrt{\sigma_T^2 + \sigma_E^2}}.$$

TABLE I. Manufacturer and product identification for major components of the experimental setup.

Component	Manufacturer	Product(s)
Laser source	Toptica	DL pro (780 nm)
Laser controller	Toptica	DLC
Wavemeter	HighFinesse	WS-7
Camera	Hamamatsu	ORCA-Flash4.0 V2
DMD + controller	Vialux	V-650L
Actuator	Newport	LTA-HS
Actuator controller	Newport	CONEX-CC
Rotation mount	Thorlabs	PRM1Z8
Rotation mount controller	Thorlabs	KDC101
Multimode fiber to wavemeter	Thorlabs	M43L02 (105 μm, 0.22 NA, 2 m)
Multimode fiber as scatterer	Thorlabs	M25L02 (200 μm, 0.22 NA, 2 m)
Polarisation maintaining fiber	Thorlabs	P3-780PM-FC-5 (5.3 μm, 0.12 NA, 5 m)
Desktop computer	Various	Xeon E5-2620 v3 CPU, 64 GB RAM

This is the square root of a Lorentzian, the same one as in Eq. (C2), and we can therefore conclude that

$$S_{\text{output}} = (S_{\text{TM}})^4.$$

APPENDIX D: EXPERIMENTAL APPARATUS

In Fig. 11, our apparatus is visually presented, and exact product identification is given for major components in Table I.

[1] J. C. Dainty, J. W. Goodman, G. Parry, T. S. McKechnie, M. Françon, and A. E. Ennos, *Laser Speckle and Related Phenomena*, 1st ed. (Springer, Berlin, 1975), Vol. 9.

[2] J. W. Goodman, *Speckle Phenomena in Optics: Theory and Applications*, 2nd ed. (SPIE, Bellingham, WA, 2020).

[3] M. Facchin, S. N. Khan, K. Dholakia, and G. D. Bruce, Determining intrinsic sensitivity and the role of multiple scattering in speckle metrology, Nat. Rev. Phys. **6**, 500 (2024).

[4] M. Facchin, K. Dholakia, and G. D. Bruce, Wavelength sensitivity of the speckle patterns produced by an integrating sphere, J. Phys. Photon. **3**, 035005 (2021).

[5] N. K. Metzger, R. Spesyvtsev, G. D. Bruce, B. Miller, G. T. Maker, G. Malcolm, M. Mazilu, and K. Dholakia, Harnessing speckle for a sub-femtometre resolved broadband wavemeter and laser stabilization, Nat. Commun. **8**, 15610 (2017).

[6] G. D. Bruce, L. O'Donnell, M. Chen, and K. Dholakia, Overcoming the speckle correlation limit to achieve a fiber wavemeter with attometer resolution, Opt. Lett. **44**, 1367 (2019).

[7] B. Redding, S. F. Liew, R. Sarma, and H. Cao, Compact spectrometer based on a disordered photonic chip, Nat. Photon. **7**, 746 (2013).

[8] Y. Wan, S. Wang, X. Fan, Z. Zhang, and Z. He, High-resolution wavemeter using Rayleigh speckle obtained by optical time domain reflectometry, Opt. Lett. **45**, 799 (2020).

[9] M. Facchin, G. D. Bruce, and K. Dholakia, Measurement of variations in gas refractive index with 10^{-9} resolution using laser speckle, ACS Photon. **9**, 830 (2022).

[10] I. Yamaguchi, A laser-speckle strain gauge, J. Sci. Instrum. **14**, 1270 (1981).

[11] M. J. Murray, A. Davis, C. Kirkendall, and B. Redding, Speckle-based strain sensing in multimode fiber, Opt. Express **27**, 28494 (2019).

[12] P. Falak, T. King-Cline, A. Maradi, T. Lee, B. Moog, P. Maniewski, R. Entwistle, M. Beresna, and C. Holmes, Ultrastable speckle-based optical fiber sensing demonstrated on an uncrewed aerial vehicle platform, Commun. Eng. **5**, 46 (2026).

[13] P. K. Rastogi, Techniques of displacement and deformation measurements in speckle metrology, in *Speckle Metrology*, edited by R. S. Sirohi, (CRC Press, Boca Raton, FL, 1993), p. 58.

[14] M. Facchin, G. D. Bruce, and K. Dholakia, Measuring picometre-level displacements using speckle patterns produced by an integrating sphere, Sci. Rep. **13**, 14607 (2023).

[15] D. Briers, D. D. Duncan, E. Hirst, S. J. Kirkpatrick, M. Larsson, W. Steenbergen, T. Stromberg, and O. B. Thompson, Laser speckle contrast imaging: Theoretical and practical limitations, J. Biomed. Opt. **18**, 66018 (2013).

[16] P. L. Falak, Q. Sun, T. Vettenburg, T. Lee, D. B. Phillips, G. Brambilla, and M. Beresna, Femtosecond Laser Written Scattering Chip for High-Resolution Low-Cost Reconstructive Spectrometry, in *Photonic Instrumentation Engineering IX*, edited by L. E. Busse, and Y. Soskind (SPIE, Bellingham, WA, 2022), Vol. 12008, p. 120080E.

[17] S. M. Popoff, G. Lerosey, R. Carminati, M. Fink, A. C. Boccara, and S. Gigan, Measuring the transmission matrix in optics: An approach to the study and control of light propagation in disordered media, Phys. Rev. Lett. **104**, 100601 (2010).

[18] M. Kim, W. Choi, Y. Choi, C. Yoon, and W. Choi, Transmission matrix of a scattering medium and its applications in biophotonics, Opt. Express **23**, 12648 (2015).

[19] S. Popoff, G. Lerosey, M. Fink, A. C. Boccara, and S. Gigan, Image transmission through an opaque material, Nat. Commun. **1**, 81 (2010).

[20] Y. Choi, T. D. Yang, C. Fang-Yen, P. Kang, K. J. Lee, R. R. Dasari, M. S. Feld, and W. Choi, Overcoming the

diffraction limit using multiple light scattering in a highly disordered medium, Phys. Rev. Lett. **107**, 023902 (2011).

[21] M. Kim, W. Choi, C. Yoon, G. H. Kim, and W. Choi, Relation between transmission eigenchannels and single-channel optimizing modes in a disordered medium, Opt. Lett. **38**, 2994 (2013).

[22] W. Choi, A. P. Mosk, Q.-H. Park, and W. Choi, Transmission eigenchannels in a disordered medium, Phys. Rev. B **83**, 134207 (2011).

[23] L. Devaud, B. Rauer, S. Mauras, S. Rotter, and S. Gigan, Correlating light fields through disordered media across multiple degrees of freedom, Phys. Rev. Res. **6**, 033265 (2024).

[24] M. W. Matthès, Y. Bromberg, J. de Rosny, and S. M. Popoff, Learning and avoiding disorder in multimode fibers, Phys. Rev. X **11**, 021060 (2021).

[25] P. Ambichl, W. Xiong, Y. Bromberg, B. Redding, H. Cao, and S. Rotter, Super- and anti-principal-modes in multimode waveguides, Phys. Rev. X **7**, 041053 (2017).

[26] J. Carpenter, B. J. Eggleton, and J. Schröder, Observation of Eisenbud-Wigner-Smith states as principal modes in multimode fibre, Nat. Photon. **9**, 751 (2015).

[27] S. Scholes, R. Kara, J. Pinnell, V. Rodríguez-Fajardo, and A. Forbes, Structured light with digital micromirror devices: A guide to best practice, Opt. Eng. **59**, 41202 (2019).

[28] R. Gutiérrez-Cuevas and S. M. Popoff, Binary amplitude holograms for shaping complex light fields with digital micromirror devices, J. Phys. Photon. **6**, 045022 (2024).

[29] S. A. Goorden, J. Bertolotti, and A. P. Mosk, Superpixel-based spatial amplitude and phase modulation using a digital micromirror device, Opt. Express **22**, 17999 (2014).

[30] R. Mouthaan, Holographic control of light propagation in optical waveguides, Ph.D. thesis, University of Cambridge, 2021.

[31] H. Zhang, B. Zhang, Q. Feng, Y. Ding, and Q. Liu, Self-reference method for measuring the transmission matrices of scattering media, Appl. Opt. **59**, 7547 (2020).

[32] K. Creath, V Phase-measurement interferometry techniques, Prog. Opt. **26**, 349 (1988).

[33] T. Gnambs, A brief note on the standard error of the Pearson correlation, Collabra Psychol **9**, 87615 (2023).

[34] H. Gee, M. Facchin, and G. D. Bruce, Data underpinning "Correlation Revival eigenmodes for differential sensitivity in speckle metrology", 2026, doi:10.17630/4a515ba3-7112-4319-b828-85f2ff276d6b.